RESEARCH ARTICLE | MARCH 20 2026

Bioaerosol transport dynamics in cold and warm environments: An experimental study using a three-dimensional-printed human airway model

Nicolás Catalán ; Salvatore Cito ; Sylvana Varela Ballesta ; Alexandre Fabregat ; Anton Vernet ; Daniel Graus ; Jordi Pallarès

Physics of Fluids 38, 031905 (2026)
https://doi.org/10.1063/5.0303143

Physics of Fluids ARTICLE pubs.aip.org/aip/pof

Bioaerosol transport dynamics in cold and warm environments: An experimental study using a three-dimensional-printed human airway model

Cite as: Phys. Fluids **38**, 031905 (2026); doi: 10.1063/5.0303143
Submitted: 19 September 2025 · Accepted: 14 February 2026 ·
Published Online: 20 March 2026

Nicolás Catalán, Salvatore Cito,[a] Sylvana Varela Ballesta, Alexandre Fabregat, Anton Vernet, Daniel Graus, and Jordi Pallarès

AFFILIATIONS

Departament d'Enginyeria Mecànica, Universitat Rovira i Virgili, Av. Països Catalans, 26, 43007 Tarragona, Spain

[a]Author to whom correspondence should be addressed: salvatore.cito@urv.cat

ABSTRACT

The COVID-19 pandemic has highlighted the critical role of respiratory aerosol dynamics in disease transmission, reinforcing the need for accurate biomedical models of exhalation and environmental dispersion. This study investigates the coupled heat and mass transfer phenomena governing bioaerosol cloud behavior during violent exhalations, such as coughing and sneezing, under varying ambient temperatures. A novel experimental setup was developed featuring a physiologically accurate, three-dimensional-printed replica of the human upper respiratory tract, including the nasal cavity, to closely replicate human exhalation mechanics and thermal conditions. Three exhalation flow rates, maintained at a body temperature of 37 °C, were tested in a climatic chamber set to ambient temperatures of 27, 17, and 7 °C. The experimental data enables an assessment of the influence of both ambient temperature and nasal airflow on aerosol dispersion. The results show that higher ambient temperatures enhance the vertical rise of the aerosol cloud and reduce ambient air entrainment, allowing the cloud to travel farther and maintain a higher particle concentration, even after the exhalation has ceased. In addition, nasal airflow alters the emission angle and modifies the subsequent trajectory of the cloud. These findings provide valuable guidance for optimizing indoor (heating, ventilation, and air conditioning) systems and serve as experimental validation for computational aerosol dispersion models.

I. INTRODUCTION

The airborne transmission of respiratory diseases has been a major public health concern, particularly highlighted during the SARS-CoV-2 pandemic. The rapid spread of COVID-19 underscored the importance of understanding how aerosolized particles behave in different environmental conditions. During violent expiratory events, such as coughing and sneezing, infected individuals release micrometer-sized droplets containing pathogens, which can remain suspended in the air and may travel over considerable distances.[1–3] These aerosolized droplets serve as a primary vector for disease transmission, especially in indoor environments where air circulation is limited.[4–6] Additionally, the onset of the pandemic during winter in the northern hemisphere, when people spend more time indoors in poorly ventilated spaces, probably facilitated the spread of the virus. The combination of low ambient temperatures, stable atmospheric stratification, and increased indoor interactions creates favorable conditions for enhanced airborne transmission risk.

Extensive research has been conducted to characterize the dynamics of aerosol dispersion from expiratory events. Previous studies have analyzed the motion and persistence of particle clouds using both human volunteers and mechanical emulators.[7–12] However, human experiments are limited by poor reproducibility due to inherent variability in exhalation intensity and duration, as well as anatomical differences between individuals.

To address these challenges, researchers have developed controlled experimental setups and numerical simulations to replicate the release of aerosols under standardized conditions.[13–22] These studies have focused on key parameters such as the exhalation velocity, the droplet evaporation, and the effects of air turbulence. While such efforts have significantly advanced our understanding of aerosol dispersion, many experiments have used simplified models of the human respiratory system, often neglecting realistic anatomical features that influence flow patterns.[20,22]

Another critical factor influencing aerosol dispersion is the role of the ambient temperature. Studies have shown that temperature gradients and buoyancy forces can significantly impact the trajectory of the aerosol clouds.[18,23–31] In quiescent indoor environments with

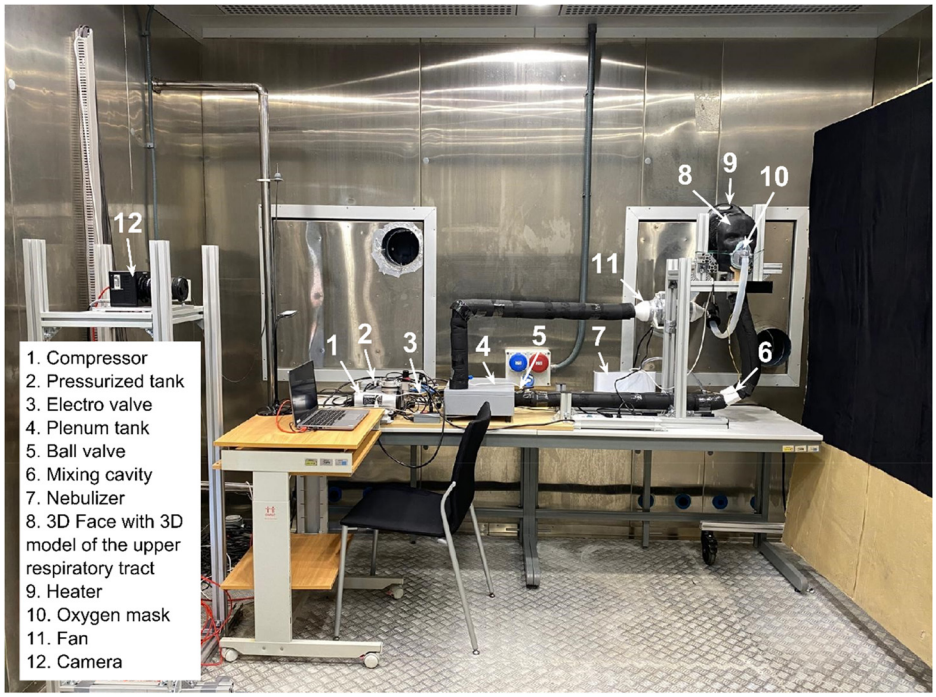

FIG. 1. Overview of the experimental setup within the climate-controlled chamber.

constant temperature, buoyancy forces drive the exhaled cloud, constituted of smaller particles, upward, while larger particles tend to settle due to gravity.[17] Investigations of thermal stratification, where temperature gradients are established between warm and cool air layers, have revealed that such effects can trap aerosols at specific heights and extend their reach up to four meters.[18] Numerical studies have further demonstrated that unstable thermal conditions, such as those created by HVAC (heating, ventilation and air conditioning) systems, promote mixing and dilution of airborne particles.[30] However, these studies have primarily focused on idealized conditions, without considering the anatomical complexity of the human upper respiratory tract, which plays a crucial role in shaping the airflow characteristics of violent expiratory events.[22]

To bridge this gap, we present an experimental study that integrates a realistic 3D-printed model of the human upper respiratory tract, including the nasal cavity, to examine aerosol dispersion under different ambient temperature conditions. Our setup allows for controlled and reproducible simulations of violent expiratory events, capturing the influence of both temperature-driven buoyancy forces and nasal airflow. By systematically varying ambient temperature and exhalation conditions, this study provides new insights into how temperature influences aerosol cloud behavior in real-world scenarios. The findings may contribute to improving indoor air quality management, refining ventilation strategies, and validating computational fluid dynamics (CFD) models for respiratory particle transport.

II. MATERIALS AND METHODS

A. Experimental setup

The experimental setup, shown in Fig. 1, consists of a compressor, a pressurized small tank with an electro valve and a relief valve, a plenum tank, a ball valve, and a pipe with a pressure differential sensor. The aerosol is generated using a nebulizer, and it is introduced in the system in a mixing chamber which is connected to a 3D-printed model of the upper respiratory tract including the nasal cavity (see Fig. 2) and a 3D-printed human face.

The intensity and the duration of the exhalation are controlled with the pressure and the position of the ball valve. The pressurized tank and the plenum tank are equipped with heaters to control the temperature of the expelled airflow. A recirculation system is used to

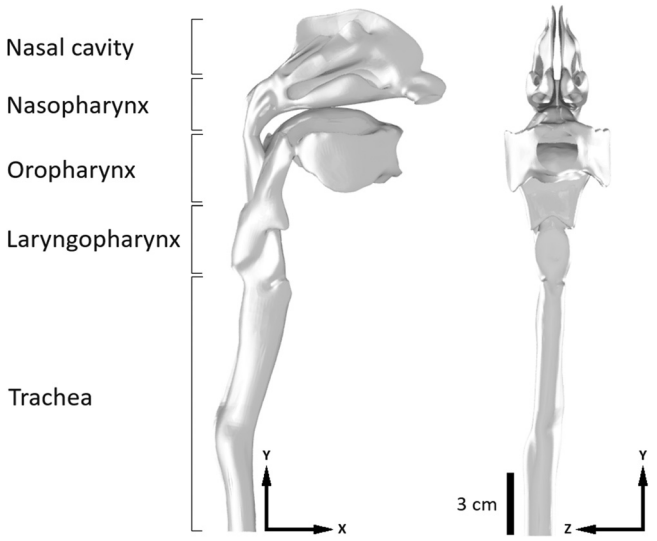

FIG. 2. 3D-printed model of the upper respiratory tract, shown from lateral and front views.

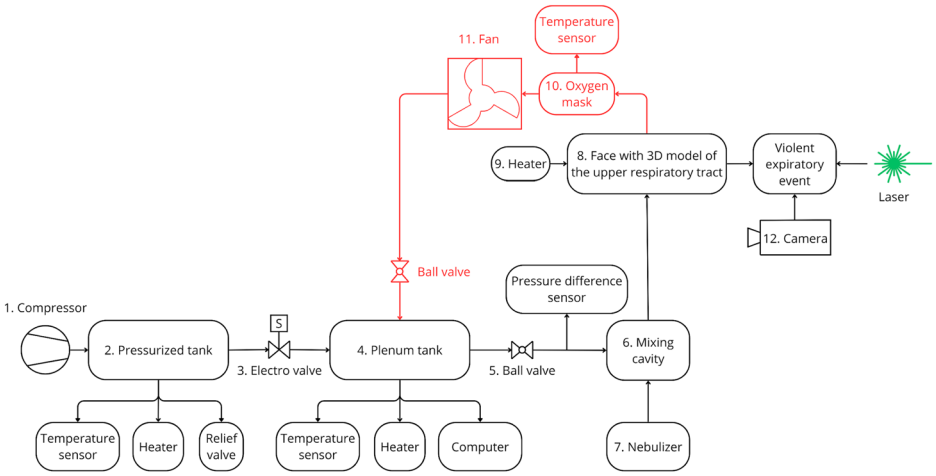

FIG. 3. Schematic representation of the recirculation system (highlighted in red), demonstrating airflow heating before exhalation.

preheat the flow before exhalation, as illustrated in Fig. 3. During the heating period, an oxygen mask is placed in the model of the face. Temperature sensors (STTS22H) were installed in the pressurized and plenum tanks, while a temperature sensor (NTCLG100E2104JB) is placed inside the oxygen mask.

Before each experiment, the system was initialized by setting the target pressure and temperature. Once stabilized, the oxygen mask was positioned over the 3D-printed face to close the circuit. A fan (TD-160/100N), connected to the plenum tank and controlled by a ball valve, was then activated to preheat the system. When all three temperature sensors reached the desired exhalation temperature, the air was compressed in the pressurized tank, and the oxygen mask was removed to initiate the expiratory event. A detailed explanation of the experimental setup can be found in Catalán *et al.*[22]

B. Temperature control and climate chamber

The experiments were conducted inside a climate-controlled chamber designed to simulate different ambient conditions. The chamber is installed in the labs of IREC (Institut de Recerca en Energia de Catalunya) in Tarragona (Spain). It has dimensions of $4.540 \times 3.400 \times 2.945\ \mathrm{m}^3$ (length × width × height) and is equipped with heating resistances, four evaporators, one axial fan, and one humidifier.

To ensure precise monitoring of environmental conditions, the chamber is equipped with thirteen temperature sensors (Model PT 100, Class A, 3-wire configuration) and a humidity sensor (Model EE99-1-FP6AD8025). These sensors are strategically distributed throughout the chamber, with one sensor placed directly next to the 3D-printed face to measure the local air temperature near the expiratory source. Atmospheric pressure was obtained from the nearest meteorological station at experiment time.

Three different ambient temperatures were tested: 27, 17, and 7 °C, and the temperature of the exhaled air was kept constant for all the experiments (37 °C). The humidity conditions were also recorded during each experiment to assess their potential influence on aerosol dispersion.

C. Measurement and data processing

Aerosols used to emulate and visualize the expelled flow were generated using a commercial nebulizer (Aroma Nebulizar 2.0). The dynamic viscosity ($5.5 \times 10^{-3} \pm 0.1 \times 10^{-3}$ Pa s) and surface tension (29.22 ± 0.01 mN/m) of the liquid used in the nebulizer were measured at ambient temperature ($T = 25\,^{\circ}\mathrm{C}$) using the TA Discovery Hybrid Rheometer and a Sigma 2000 tensiometer, respectively. The size distribution of the aerosol particles was measured with a HandiLaz Mini II airborne particle counter. The predominant particle size is around in 1 μm, which is close to the smallest airborne droplets generated during violent expiratory events. To visualize and quantify the aerosol cloud evolution, a 5-mm-thick laser sheet was generated using a continuous green laser (CNI Model PSU-W-LED MGL-W-532, wavelength: 532 nm). The laser illuminated the symmetry xy-plane of the flow (see Fig. 2 which includes the adopted system of reference).

Images were captured using a Photron FASTCAM Mini UX100 high-speed digital camera, operating at 50 frames per second (FPS) with a resolution of 1 280 pixels × 1 024 pixels over a duration of 4 s. The camera's field of view covered an area of $1.30 \times 1.04\ \mathrm{m}^2$, ensuring full tracking of the particle cloud dynamics. The resulting equivalence is 1.02×10^{-3} m pixel^{-1}.

Post-processing was performed using an in-house MATLAB script. The images were binarized using a manually selected threshold, which was kept constant for all experiments. Calibration was performed by imaging a reference object of known dimensions and averaging several measurements to obtain the meter-to-pixel conversion factor. Additional details of the image processing procedure are provided in Appendix A. The cloud centroid coordinates (c_x, c_y), as well as the horizontal (σ_x) and vertical (σ_y) extents of the aerosol cloud, were calculated using the standard deviation of illuminated pixels, as defined by the following equations:

$$c_x = \frac{\sum_{i=1}^{n} x_i}{n}, \qquad c_y = \frac{\sum_{i=1}^{n} y_i}{n} \tag{1}$$

$$\sigma_x = \sqrt{\frac{\sum_{i=1}^{n} (x_i - c_x)^2}{n}}, \qquad \sigma_y = \sqrt{\frac{\sum_{i=1}^{n} (y_i - c_y)^2}{n}} \tag{2}$$

where n is the number of illuminated pixels in the binarized image, and x_i and y_i represent the horizontal and vertical pixel positions, respectively.

Each experimental case was repeated ten times to evaluate the intrinsic variability of the resulting turbulent flow. The mean and

TABLE I. Summary of experimental conditions, including flow rates, exhalation duration, and nostril openness.

	Total flow rate (l/s)		Duration (s)	Max velocity (m/s)	Nostrils	
Code	Max.	Av.	t_d	Mouth	Closed	Open
ΔTiF1N0	3.75	1.29	0.52	11.94	X	
ΔTiF1N1						X
ΔTiF2N0	4.40	1.72	0.44	14.01	X	
ΔTiF2N1						X
ΔTiF3N0	5.01	2.04	0.34	15.95	X	
ΔTiF3N1						X

standard deviation of the cloud trajectory and dispersion were calculated for each combination of exhalation flow rate and ambient temperature. For validation, the measured time evolutions of the exhalation flow rate were compared against published experimental data reported by Gupta *et al.*,[7] ensuring consistency with existing literature on human expiratory events.

III. RESULTS AND DISCUSSION

A. Experimental results

To investigate the effect of buoyancy, the nasal cavity flow, and the exhalation strength and duration, we conducted eighteen different experimental cases, as listed in Table I. Cases are labeled as $\Delta TiFjNk$, where $i = 1, 2, 3$ corresponds to ambient temperatures of 27, 17, and 7 °C, respectively (i.e., increasing temperature difference between the exhaled 27°C air and the ambient temperature), $j = 1, 2, 3$ denotes the exhalation flow rate level (with 1 being the lowest and 3 the highest flow), and $k = 0$ for closed nostrils or 1 for open nostrils. For instance, $\Delta T3F2N0$ denotes the case with the coldest ambient (7 °C), the medium flow rate, and with the nostrils closed. Table I presents for each case the total flow rate, the exhalation duration, the maximum velocity, and the nostril openness. As indicated above, the results for each case presented and discussed in this section are obtained from the ensemble average of the 10 realizations.

1. Flow rate profiles and validation

Figure 4 shows the ensemble-averaged time evolutions of the exhalation flow rate for the three different test conditions ($F1$, $F2$, and $F3$). The shaded areas indicate ± 5% variability based on sixty independent trials. The solid lines represent the measured flow rates generated with the simulator, while the dashed lines denote the envelope of the different measurements using volunteers reported by Gupta *et al.*[7] in their Fig. 3. The measured time evolutions lay between the measurements, demonstrating the reliability of the compressor-driven expiratory event emulator. The maximum exhalation velocity increased with flow rate, with $F3$ exhibiting the highest velocity and shortest duration, while $F1$ produced a slower, more sustained airflow.

Different temperatures have been considered to study the effect of buoyancy on the plume generated by violent expiratory events. The chosen temperature of the simulator is $T = 37$ °C, simulating body temperature conditions in SARS-CoV-2 infected people.[32] Three

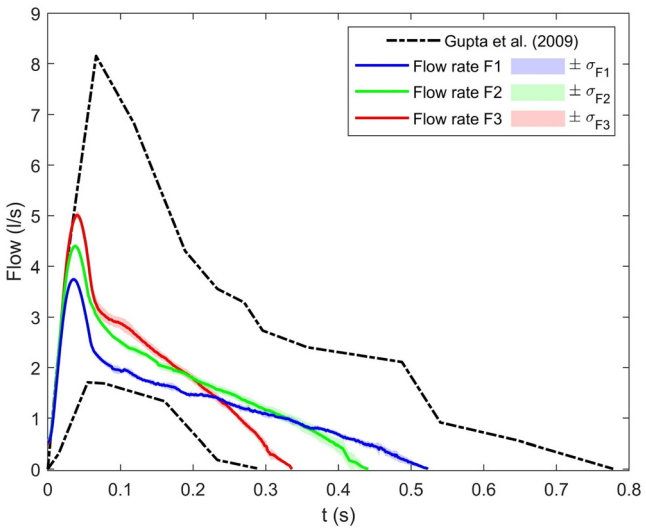

FIG. 4. Temporal evolution of the ensemble-averaged volumetric flow rate for the three experiments (solid lines), with standard deviation (shaded areas) and comparison to reference data from Gupta *et al.*[7] (dashed lines) which are digitized and replotted for comparison.

different temperatures were selected, $\Delta T1 = 10$, $\Delta T2 = 20$, and $\Delta T3 = 30$ °C. Table II shows the average temperatures of the climatic chamber for each case during the experiments, the temperature near the face for better control, the relative humidity and the atmospheric pressure, as well as the standard deviation of all measurements.

2. Centroid trajectories and nasal cavity influence

The trajectory of the centroid of the aerosol cloud was analyzed to determine the impact of the nasal airflow and ambient temperature. Figure 5 shows the ensemble-averaged centroid trajectories during 4 *s* for all test cases, with dashed lines representing closed nostrils ($N0$) and solid lines indicating open nostrils ($N1$). Figures 5(a)–5(c) illustrate the evolution of the centroids for the three different values of the temperature increment, $\Delta T1$, $\Delta T2$, and $\Delta T3$, respectively. As a reference, isothermal results from Catalán *et al.*[22] were added in black with a duration of 1.5 s. The results indicate that nasal airflow modifies the downward trajectory of the expelled particle cloud. With closed nostrils ($N0$), the centroid follows a 16° steep downward path, while open nostrils ($N1$) divert part of the airflow upwards, reducing the angle, with respect to the horizontal, to 32°. The geometry of the respiratory tract considered the open area of the mouth (3.14×10^{-4} m^2) is circular with a diameter of 0.02 m and the total area of the two nostrils is

TABLE II. Experimental measurements.

Case	ΔT (°C)	Average room T (°C)	Average face T (°C)	RH (%)	Atmospheric pressure (hPa)
ΔT1	10	27.6 ± 0.6	28.3 ± 0.8	39 ± 6	1 022 ± 7
ΔT2	20	16.9 ± 0.5	18.6 ± 0.8	54 ± 5	1 026 ± 3
ΔT3	30	7.0 ± 0.1	9.3 ± 0.3	44 ± 4	1 011 ± 7

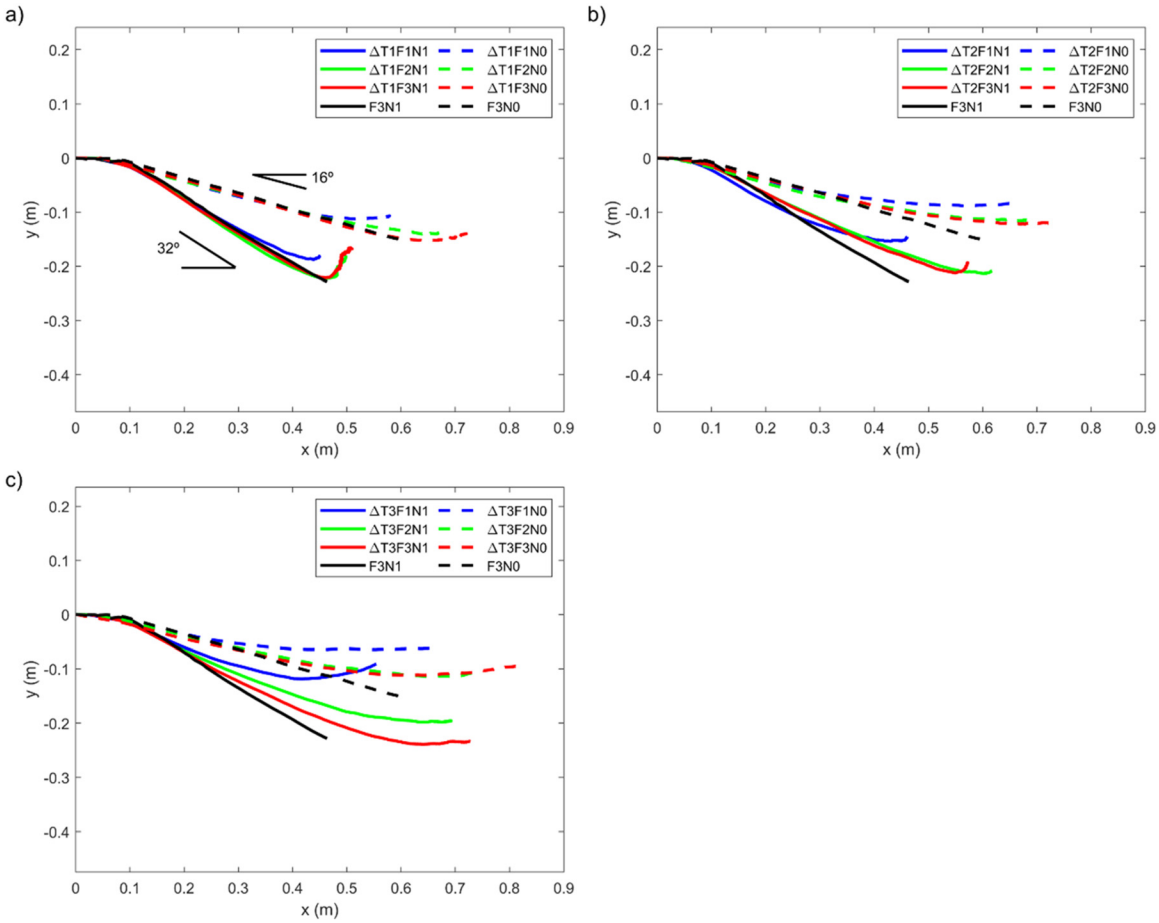

FIG. 5. Ensemble-averaged centroid trajectories obtained from ten independent experimental realizations. Panels (a), (b), and (c) correspond to $\Delta T1$, $\Delta T2$, and $\Delta T3$, respectively. Note that black lines, added as reference, represent the isothermal cases from Catalán *et al.*[22]

$1.99 \times 10^{-4}\,\mathrm{m}^2$. When the nostrils are open, the total flow rate is distributed approximately proportionally between the open areas of the mouth and nostrils, with 61% passing through the mouth and 39% through the nostrils. At sufficiently large times, the centroid position of the cloud with the nostrils closed is above the centroid with the nostrils open by about 0.1–0.15 m.

These inclination angles evolve over time due to buoyancy forces. In Fig. 5(a), the effects of these forces are more noticeable when inertial forces are smaller. The influence of ambient temperature is also evident; indeed, as the temperature difference increases, buoyancy forces alter the angle of the particle cloud, as shown in Figs. 5(b) and 5(c). The centroid displacements observed in the experiments are approximately one order of magnitude larger than the estimated centroid position uncertainty (± 0.01 m), indicating that the reported trends are well above the measurement noise.

3. Inertial vs buoyant forces: Richardson number analysis

The interplay between inertial and buoyancy forces in expiratory flows can be examined through their characteristic timescales. The inertial characteristic time can be defined as $t_{in} = \frac{D}{U}$, where D is the mouth diameter (m) and U is the velocity of the particle cloud tip (m/s). This timescale represents the duration over which inertial forces dominate, and it varies dynamically with the velocity profile of the expiratory event. In contrast, the buoyancy characteristic time t_b (s) can be defined as

$$t_b = \sqrt{\frac{D}{g\beta\Delta T}} \tag{3}$$

where g is the gravitational acceleration ($\mathrm{m/s^2}$), β is the thermal expansion coefficient evaluated at the mean temperature of the exhaled and ambient air ($1/K$), and ΔT is the temperature difference (K) between the exhaled air and the environment. The values of t_b decrease with increasing ΔT, indicating the buoyancy effects are faster for large temperature differences.

At the onset of exhalation, t_{in} is significantly smaller than t_b, confirming that inertial forces govern the initial phase of the flow. As the exhalation progresses and velocity decreases, t_{in} increases and approaches t_b, producing a gradual transition toward buoyancy-influenced flow. To quantify the relative importance of

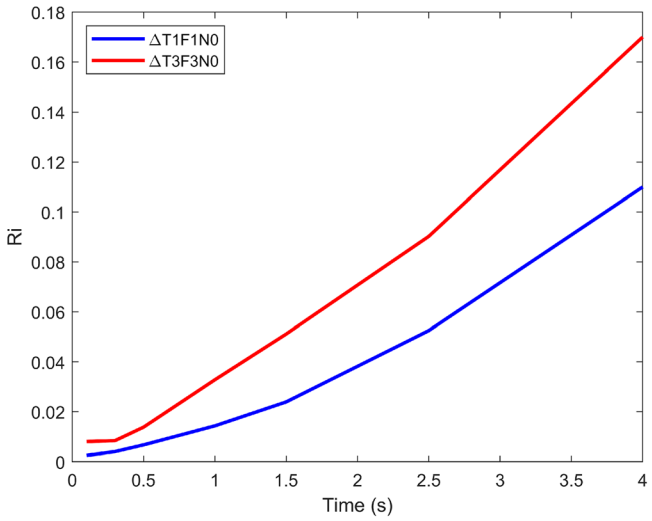

FIG. 6. Evolution of Richardson number over time in cases $\Delta T1F1N0$ and $\Delta T3F3N0$.

the inertial and buoyant forces, the Richardson number (Ri) can be defined as

$$Ri = \left(\frac{t_{in}}{t_b}\right)^2 = \frac{g\beta\Delta TD}{U^2} = \frac{Gr}{Re^2} \tag{4}$$

The Richardson number characterizes the relative influence of buoyancy vs inertia. Figure 6 shows the evolution of the Richardson number over time for cases $\Delta T1F1N0$ and $\Delta T3F3N0$, with the most extreme cases being those with the lowest flow rate and ΔT vs those with the highest flow rate and ΔT. Note that the Richardson number increases with time because the velocity of the tip of the cloud progressively decreases. At early times, $Ri \ll 1$, indicating a shear-dominated regime, while later stages exhibit increasing Ri, particularly for larger temperature differences, suggesting enhanced buoyancy effects. However, even at higher ΔT, Ri remains below 0.18, highlighting expiratory flows are predominantly driven by inertia rather than buoyancy. At higher ΔT (colder ambient), Ri increases more rapidly, indicating an earlier onset of the buoyancy effects. At lower ΔT (i.e., in warmer ambient conditions), the Richardson number Ri remains low for a longer duration, indicating that inertia effects persist over an extended period. This emphasizes that buoyancy plays a secondary role initially but becomes more relevant as the exhalation slows down, particularly in colder environments. This indicates that the initial jet momentum largely governs the short-term spread of the particle cloud (during the first 1–2 s) and buoyancy plays a secondary role until the jet has slowed down sufficiently.

Humidity effects were not included in the calculation of the Richardson number, as the expelled flow is dominated by inertia and temperature-induced buoyancy, while humidity-induced density variations are comparatively small. The aerosol microdroplets were employed exclusively as flow tracers to visualize the expelled air jet. Although they do not reproduce the full physicochemical complexity of real respiratory droplets, particles in the submicron–micron size range are transported by the flow in a comparable manner, since their dynamics are dominated by aerodynamic drag. The tracer particles are advected by the violent expiratory flow, and even if partial evaporation were to occur, the associated increase in humidity would enhance buoyancy effects and thus increase the Richardson number, making the present estimates conservative.

4. Cloud size and spread over time

The growth and spread of the aerosol cloud were analyzed using the cloud extents (σ_x, σ_y) in both horizontal and vertical directions. Figure 7 shows the time evolution of the cloud sizes, with comparisons between flow rates $F1$ and $F2$, and nostril conditions $N0$ (closed) and $N1$ (open). The middle solid line corresponds to the centroid ($c_{x,y}$) position, while the dashed and dotted line denotes $c_{x,y} \pm \sigma_{x,y}$, corresponding to the cloud extension. Figures 7(a) and 7(b) use elapsed time as the vertical axis, while shaded areas indicate one standard deviation for an ensemble of 10 experimental realizations.

Results indicate that a higher flow rate ($F2$) increases the horizontal spread, with the particle cloud traveling farther along the x axis and exhibiting slightly greater variability across experiments, as shown by the wider shaded area. In the vertical direction [Figs. 7(c) and 7(d)], the larger flow rate in $F2$ leads to a lower vertical position compared to the smaller flow rate, $F1$.

The presence of nasal airflow ($N1$) primarily affects the vertical position of the particle cloud, with $F2$ showing a difference of approximately 0.1 m between closed ($N0$) and open ($N1$) nostrils. This highlights how nasal airflow modifies the initial momentum distribution of the exhaled particles. When the nasal airways are open ($N1$), part of the exhaled air is diverted through the nose, reducing the overall momentum of the main exhaled jet. As a result, buoyancy forces act more effectively and earlier, accelerating the vertical rise of the particle cloud compared to the closed airway ($N0$) case, where the full momentum is directed through the mouth, delaying buoyancy effects. This phenomenon is particularly evident in $F2$, where the presence of nasal airflow leads to an increased vertical displacement of approximately 0.1 m.

Table III and Fig. 7(b) provide a detailed comparison of the ratios of the particle cloud positions and sizes along the axial (horizontal) direction for different flow rates, under both closed ($N0$) and open ($N1$) nasal airway conditions. The results show that the horizontal scaling closely aligns with the flow rate ratios, with a maximum error of 14%. This consistency suggests that the horizontal displacements are primarily influenced by momentum and initial flow conditions, making it a reliable predictor of cloud size ratios across varying flow rates. In contrast, a similar scaling relationship is not observed in the vertical direction. Vertical displacement is influenced by additional factors, including buoyancy forces and the effects of nasal airflow. For instance, if the nostrils are open ($N1$) there is a reduction of the initial momentum of the exhaled particles, enhancing the role of buoyancy forces and leading to greater vertical displacement compared to the case of closed nostrils ($N0$). These combined effects disrupt the straightforward relationship between flow rates and vertical cloud sizes observed in the horizontal direction. Despite these complexities, the scaling framework presented in Table III provides a useful starting point for estimating particle cloud sizes across different flow rates. The results highlight the importance of considering both horizontal and vertical dynamics when predicting particle dispersion under varying conditions.

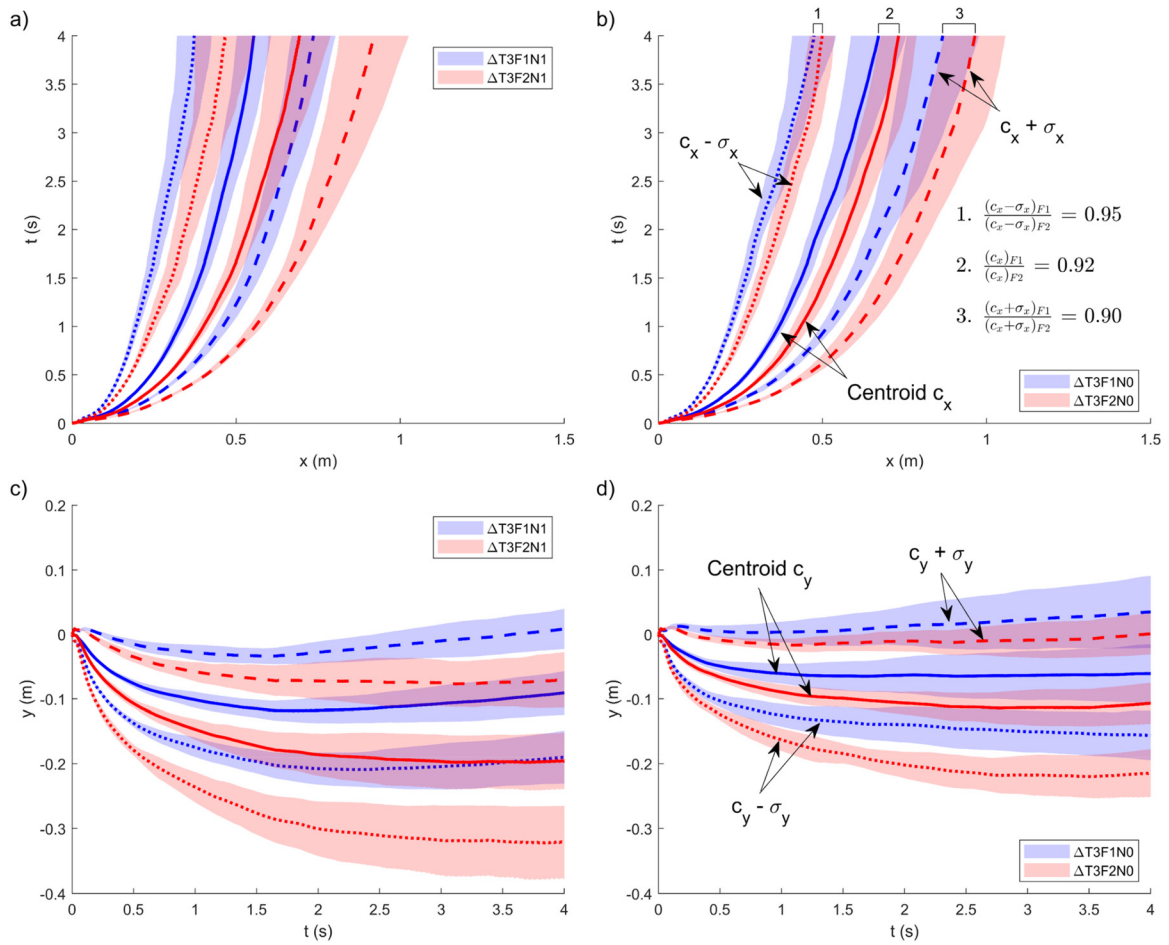

FIG. 7. Tracking of the position of the ensemble-averaged centroid and time evolutions of the sizes of particle clouds in x axis and y axis for cases $\Delta T3F1N1$ and $\Delta T3F2N1$ (a) and (c), and $\Delta T3F1N0$ and $\Delta T3F2N0$ (b) and (d). Panel (b) shows the ratio between the sizes of the cases analyzed. Shaded areas indicate ± one standard deviation from an ensemble of ten independent experimental realizations.

TABLE III. Flow rate ratio and difference of the distances of the puff between the cases compared at different temperatures.

Code	Difference Temperature	Flow rate ratio	N0			N1			Size ratio avg.	Difference % in abs. value
			$c_x - \sigma_x$ ratio	c_x ratio	$c_x + \sigma_x$ ratio	$c_x - \sigma_x$ ratio	c_x ratio	$c_x + \sigma_x$ ratio		
F1/F2	ΔT1	0.86	0.87	0.86	0.86	0.91	0.90	0.90	F1 = 0.88F2	2
F1/F3		0.75	0.78	0.80	0.81	0.93	0.89	0.87	F1 = 0.85F3	10
F2/F3		0.88	0.90	0.93	0.95	1.03	0.98	0.97	F2 = 0.96F3	8
F1/F2	ΔT2	0.86	1.05	0.99	0.95	0.70	0.75	0.77	F1 = 0.87F2	1
F1/F3		0.75	0.99	0.93	0.90	0.83	0.80	0.79	F1 = 0.87F3	12
F2/F3		0.88	0.94	0.94	0.94	1.19	1.08	1.03	F2 = 1.02F3	14
F1/F2	ΔT3	0.86	0.95	0.92	0.90	0.80	0.80	0.80	F1 = 0.86F2	0
F1/F3		0.75	0.87	0.82	0.80	0.82	0.76	0.74	F1 = 0.80F3	5
F2/F3		0.88	0.91	0.90	0.89	1.02	0.95	0.92	F2 = 0.93F3	5

Figure 8 further compares cloud centroid trajectories (solid and dashed lines), and the particle cloud sizes (crosses showing the extents in the x and y axes at three specific positions) over time for flow rates $F1$ and $F3$, under open ($N1$) and closed ($N0$) nasal airways conditions, and at different ambient temperature differences ($\Delta T1$ and $\Delta T3$).

For flow rate $F1$, the centroid trajectories show minimal differences between open and closed nostrils along the axial (x) direction. However, the vertical (y) trajectories reveal a slight downward shift in the presence of nasal airways ($N1$), reflecting reduced vertical displacement of the particle cloud when part of the exhaled flow is diverted through the nose. Additionally, larger ΔT (colder ambient) results in more pronounced vertical lifting due to stronger buoyancy effects while smaller ΔT (warmer ambient) allows the cloud to spread more horizontally, maintaining a broader lateral dispersion. Indeed, for the relatively homogeneous 1 μm particles, buoyancy counteracts their downward momentum while uniformly enhancing their upward motion. This cohesive upward movement reduces the vertical divergence of the particles, resulting in a more concentrated cloud and an apparent reduction in vertical spread.

In the case of flow rate $F3$, the centroid trajectories exhibit a larger spread compared to $F1$, both horizontally and vertically, reflecting the higher initial momentum associated with the increased flow rate. The particle cloud sizes (crosses) also indicate greater extents in both directions, particularly under $N0$ conditions, where the full

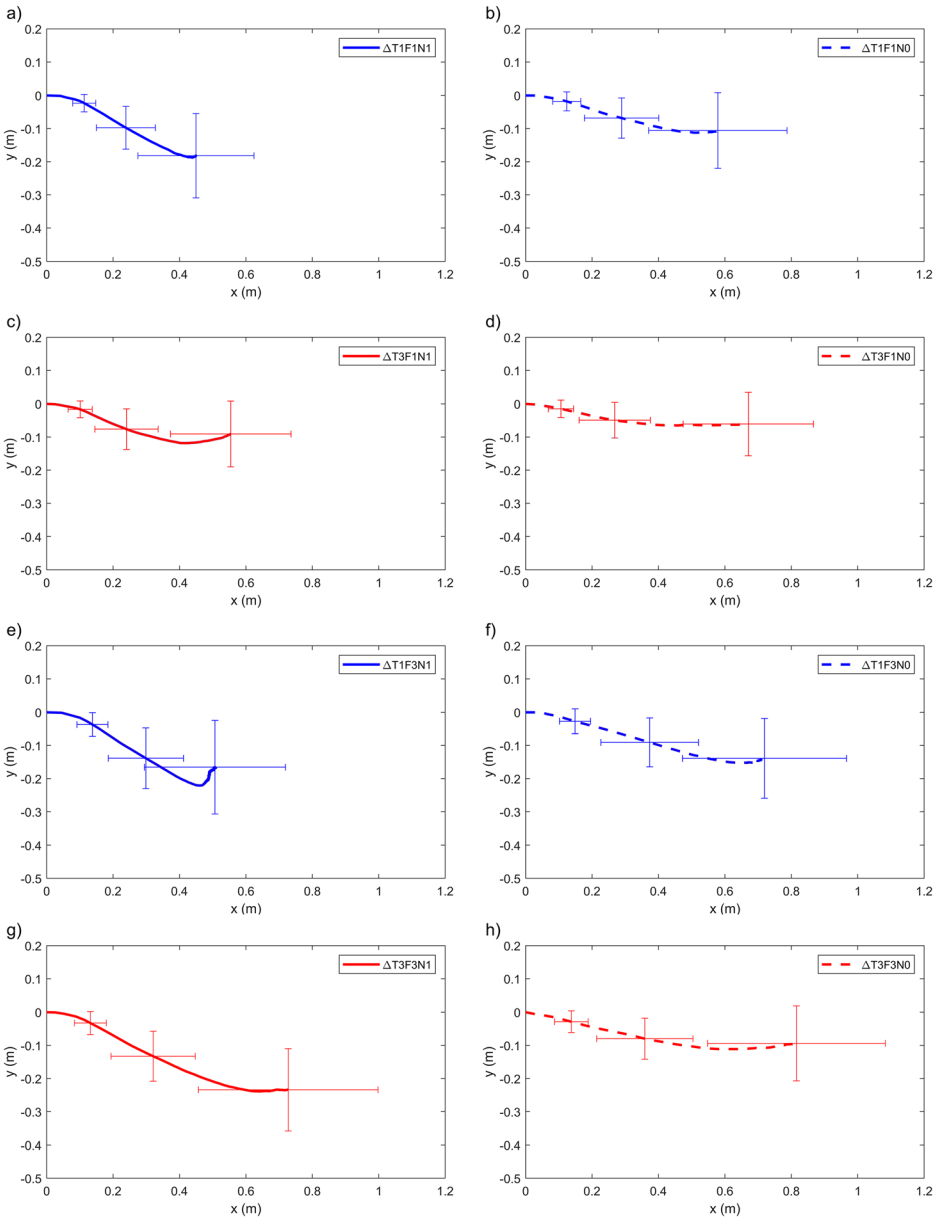

FIG. 8. Centroid trajectories of the expelled flow for F1 and F3 configurations under different ambient temperature differences and nostril conditions. Panels (a)–(d) correspond to F1 and (e)–(h) to F3. Solid lines indicate open-nostril cases (N1) and dashed lines closed-nostril cases (N0). Blue curves correspond to ΔT1 and red curves to ΔT3. Symbols represent the measured centroid positions, with horizontal and vertical error bars indicating the spatial spread of the particle cloud in the x- and y-directions, respectively.

momentum of the exhaled flow drives larger dispersion. As with $F1$, increasing ΔT leads to uniform lift of the particle cloud due to buoyancy forces, but does not fully counteract the enhanced dispersion caused by the larger flow rate. Figure 8 highlights how flow rate, nasal airways, and temperature differences jointly influence the centroid trajectories and particle cloud sizes. Higher flow rates amplify particle dispersion, while nasal airways and thermal forces modulate the vertical displacement and cloud extension.

Figure 9 (Multimedia view) presents snapshots of the aerosol cloud at different time intervals for the cases the cases $\Delta T1F1N0$ and $\Delta T3F1N0$, visually confirming the temperature-dependent differences in the dispersion behavior. As discussed in the evolution of the cloud centroid, shown in Fig. 7, the particle cloud under higher temperature differences ($\Delta T3$) tends to exhibit less dispersion and retains more of its initial structure. The increased temperature difference between the expelled flow and the ambient air reduces the entrainment of surrounding air into the particle cloud, thereby limiting its dispersion.

This phenomenon is consistent with the findings of Soteriou and Ghoniem,[33] which demonstrated that density ratios between the injected flow and the surrounding environment significantly impact shear layer dynamics. A higher density ratio, as observed in the $\Delta T3$ case, promotes greater jet stability by inhibiting the roll-up and mixing vortices in the shear layer of the jet. This leads to reduce the denser background flow entrainment and a more coherent, less turbulent, particle cloud structure. Additionally, Fig. 9 suggests that the case with a higher temperature difference ($\Delta T3$), exhibits greater particle concentration, as evidenced by the increased brightness of the illuminated cloud. The higher particle density in the aerosol-laden flow allows it to travel longer distances while maintaining elevated particle concentrations, which could increase the potential risk of disease transmission. Figure 8 shows that the range of the clouds for the largest temperature difference ($\Delta T3 = 30\,^{\circ}\mathrm{C}$) increases by about 0.1 m in comparison with the cases corresponding to the smaller temperature difference ($\Delta T1 = 10\,^{\circ}\mathrm{C}$).

B. Comparison with theoretical models

Theoretical models available in the literature provide predictions for the temporal evolution of particle clouds. Pallarès and Fabregat[34] developed a theoretical model inspired by the works of Abani and Reitz,[35] which predicts particle cloud size and travel distance, and Richards,[36] which describes the evolution of buoyancy forces. The model integrates these concepts to estimate particle cloud behavior through an entrainment coefficient $K = 0.24$, as defined in Pallarès and Fabregat.[34]

Figure 10 compares the experimental cases $\Delta T2F3N0$ [Fig. 10(a)] and $\Delta T3F3N0$ [Fig. 10(b)] with predictions from the theoretical model at $t = 4$ s. The experimental conditions were used to calculate the theoretical trajectory of the centroid using the areas of the triangle and circle shown in Fig. 10. The entrainment coefficient K was derived from the study by Catalán *et al.*[22] for the case $F3N0$. Note that the range x' and the vertical diameter D_v of the cloud are shown in Fig. 10(b). The radius of the frontal puff (R_p) is also indicated (see Pallarès and Fabregat[34] for more details). Our data suggests that using an entrainment coefficient calibrated for one condition $F3N0$ in the theoretical model yields reasonable predictions across other conditions, but with a systematic overshoot in extent (~10%–15% larger than observed). This kind of validation is important for modeling, as it quantifies the model's accuracy and limitations. Indeed, although the theoretical model slightly overestimates the size of the particle cloud, it provides a reasonable approximation of the overall size and evolution of the particle cloud. This discrepancy can be attributed to assumptions in the model, such as idealized entrainment dynamics and uniform buoyancy effects, which may not fully capture the complexity of real-world conditions. Despite these limitations, the model offers valuable insight into the general behavior and progression of particle clouds under various thermal and flow conditions.

Figure 11 shows a snapshot of the particle cloud corresponding to the case $\Delta T3F3N0$ at $t = 0.5$ s. The position of the particle cloud tip is defined along the x' variable, representing the distance from the mouth to the farthest point of the cloud. The expression derived by Catalán *et al.*[22] (depicted in Fig. 12) provides a non-dimensional analysis of the particle cloud tip's position as a function of time, scaled by the average flow exit velocity. This expression incorporates various flow rates, geometrical configurations (presence or absence of nasal cavities), and temperature differences. Despite minor discrepancies in shorter times, the model accurately predicts the non-dimensional evolution of the particle cloud tip, demonstrating its robustness to varying conditions.

Buoyancy forces are observed to modify the orientation of the particle cloud. The angle of the particle cloud (α) is defined as the angle between the horizontal axis (x axis) and the line connecting the mouth to the centroid of the particle cloud. To characterize this angle, we computed its tangent, given by

$$\tan\alpha = \frac{c_y}{c_x}, \tag{5}$$

where c_x and c_y are the coordinates of the cloud centroid to the mouth.

The results shown in Fig. 13 depict the evolution of the tangent of the angle as a function of average velocity scaled by D/t. For the isothermal case [Fig. 13(a)], the tangent initially decreases as the cloud expands, but no consistent plateau is observed. Instead, data points exhibit a gradual reduction in variability, suggesting that without thermal effects, the trajectory remains more stable over time. For cases with temperature differences [$\Delta T1$, $\Delta T2$, *and* $\Delta T3$, Figs. 13(b)–13(d)], the tangent follows a more dynamic evolution, reflecting the increasing influence of buoyancy forces. Higher temperature differences ($\Delta T3$) lead to a lower tangent value, as buoyancy enhances vertical displacement, shifting the centroid upward. This behavior aligns with the findings of Soteriou and Ghoniem,[33] which demonstrated that a higher density contrast between the jet and its surroundings stabilizes the shear layer, reducing vortex roll-up and entrainment. In the $\Delta T3$ case, the expelled air, significantly warmer and therefore less dense than the ambient air, increases the density ratio. This stabilization effect reduces turbulent fluctuations at the cloud boundaries, thereby limiting lateral spreading. In other words, a large temperature difference (a much colder room) causes the jet to rise more and spread less laterally, keeping the cloud more intact.

As a result, the particle cloud retains its initial structure more effectively and follows a more coherent trajectory over time. The reduced lateral dispersion can be understood because of this stabilized flow, where buoyancy suppresses shear-driven mixing, leading to a more predictable and less diffusive trajectory. Consequently, the

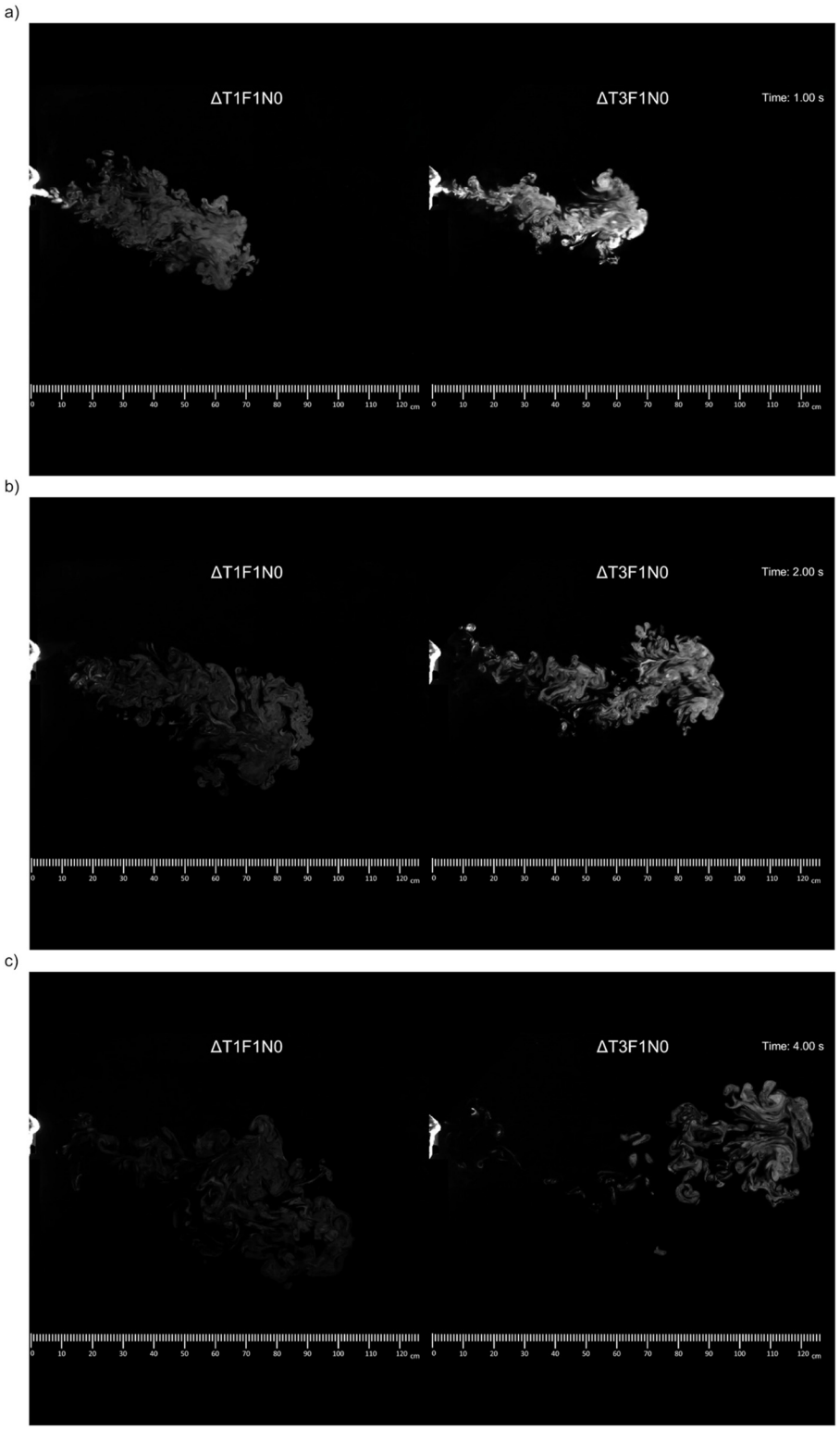

FIG. 9. Snapshots at $t = 1$ (a), $t = 2$ (b), and $t = 4$ s (c) of cases $\Delta T1F1N0$ and $\Delta T3F1N0$. Multimedia online available.

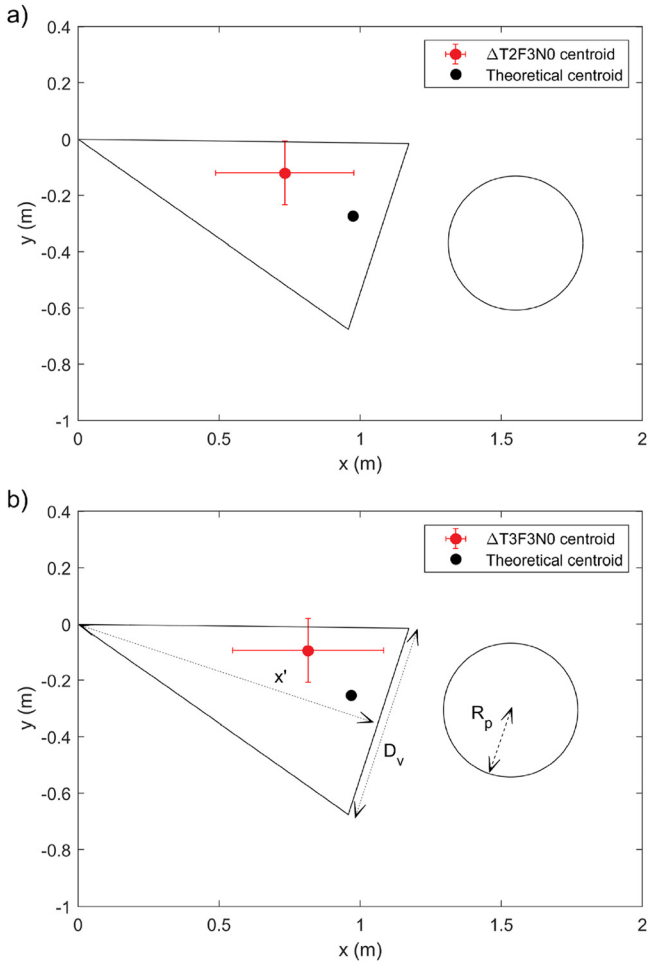

FIG. 10. Comparison of the locations of the cloud centroid observed experimentally and theoretically predicted at $t = 4$ s. Red circles indicate the experimental centroid, while black circles represent the theoretical centroid obtained from the cone and circular models using the entrainment coefficient reported by Catalán *et al.*[22] Panel (a) corresponds to case $\Delta T2F3N0$ case and panel (b), to case $\Delta T3F3N0$.

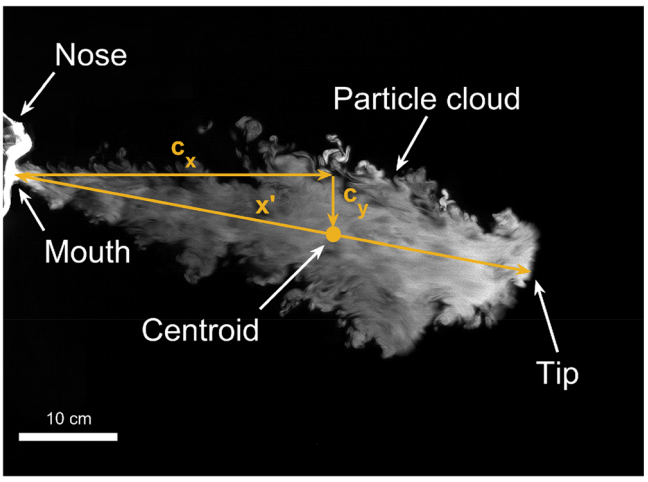

FIG. 11. Definition of c_x, c_y, and x' coordinates of case $\Delta T3F3N0$ at $t = 0.5$ s.

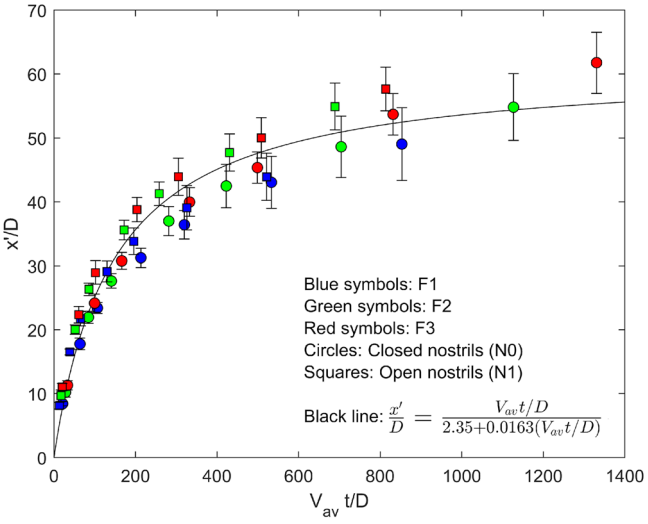

FIG. 12. Non-dimensional time evolution of the range of the cloud along the direction of the centroid. Error bars indicate the standard deviation of the mean computed from ten independent experimental realizations.

evolution of the tangent value remains lower, as the centroid's movement is more constrained within a defined path.

The presence of nasal airflow ($N1$) introduces additional variability in the tangent evolution, but its influence depends on the flow rate and temperature conditions. In some cases, nasal airflow enhances vertical dispersion, while in others, it appears to slightly suppress variations in the centroid trajectory.

IV. CONCLUSIONS

A novel machine was developed to simulate violent expiratory events using a realistic upper respiratory tract that includes the nasal cavity. We have chosen three different flow rates with a 37 °C temperature under three different background temperature (27 17, and 7 °C) to investigate the dynamics and dispersion of the aerosol cloud during $t = 4$ *s*. The three-flow rates tested significantly affected the distance the particle cloud traveled. The higher the flow rate, the greater the distance traveled by the particle cloud. The flow through the nasal cavity modifies the centroid's angle with respect to the horizontal axis and the shape of the particle cloud. The centroid trajectory is inclined downward by 32° with open nostrils and 16° with closed nostrils. These angles are not constant due to buoyancy forces; however, when inertial forces are predominant, the trajectory of the particle cloud keeps these values of the angle, essentially, constant.

Buoyancy forces cause the particle cloud to rise vertically as ambient temperature increases. This effect is visible in the 2 configurations analyzed, with open and closed nostrils. On the other hand, the rise of temperature reduces the entrainment in the aerosol cloud, reaching greater distances with a higher particle concentration, as described in Soteriou and Ghoniem.[33] This effect was observed in all cases, regardless of the role of the nasal cavity or the value of the flow rate. The

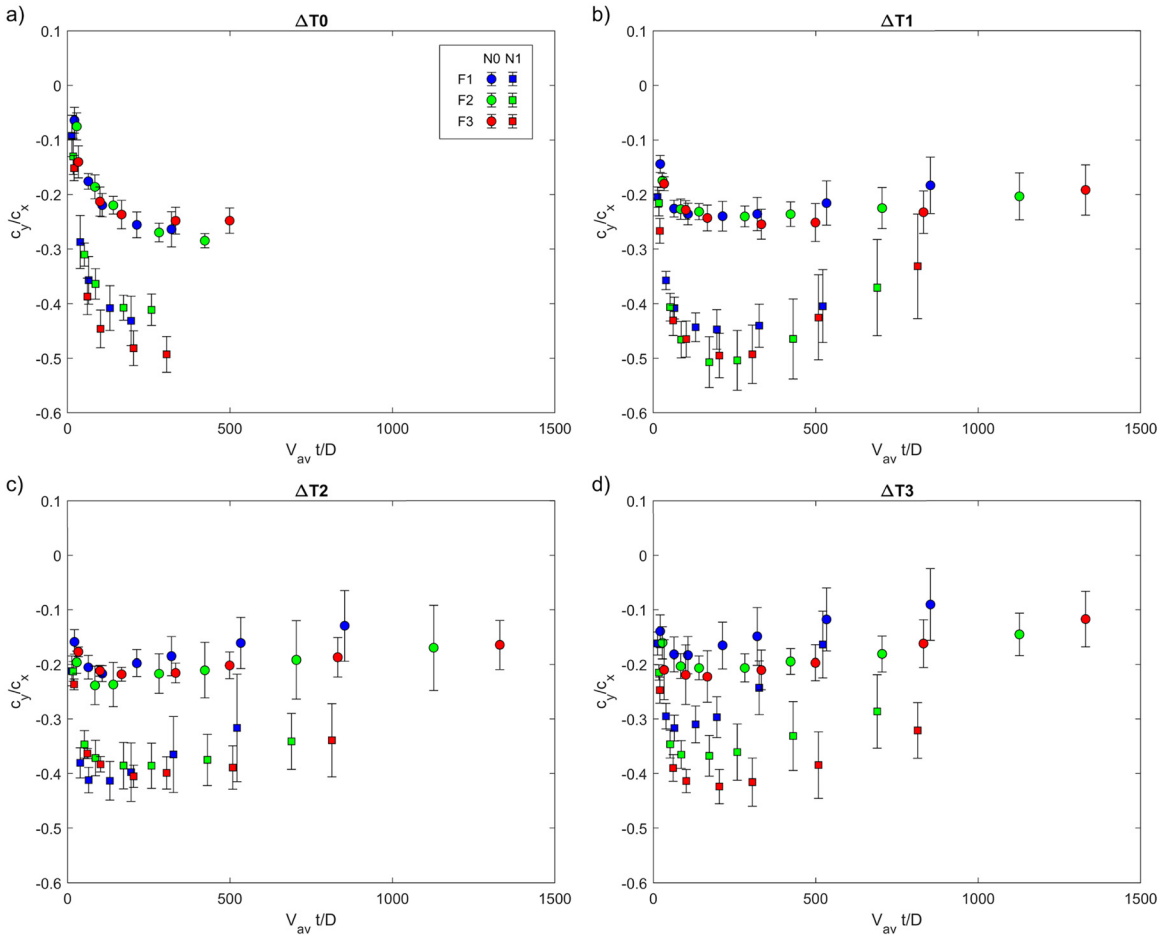

FIG. 13. Non-dimensional time evolution of the range of the cloud along the tangent of the angle for the isothermal case from Catalán *et al.*[22] (a), and cases $\Delta T1$ (b), $\Delta T2$ (c), and $\Delta T3$ (d). Error bars indicate the standard deviation of the mean computed from ten independent experimental realizations.

particle cloud size is similar across cases with identical conditions, regardless of temperature differences. We observe a slight lateral "squeezing" of the cloud under the highest thermal difference, likely due to buoyancy.

The theoretical model developed by Pallarès and Fabregat[34] overpredicts the size and the distance reached of the particle cloud compared with the experimental results. In contrast, this theoretical model is a rapid way to calculate aerosol exposure and can provide a general idea of the size and distance reached. The derived expression in Catalán *et al.*[22] predicts accurately the particle cloud tip x' in all conditions in different temperatures. This expression could give a general idea of the distance reached of the aerosol cloud and is not necessary to calculate the entrainment coefficient K as in the theoretical model provided by Pallarès and Fabregat.[34]

The experimental methodology was intentionally limited to two-dimensional measurements, which are sufficient to capture the dominant dynamics in the plane and address the specific objectives of this work. However, possible off-plane effects and three-dimensional structures cannot be fully resolved within this framework. A complete three-dimensional analysis would require the implementation of stereoscopic or volumetric measurement techniques, such as stereoscopic particle image velocimetry (PIV) or tomographic approaches, which are left for future research.

The study's findings emphasize the critical role of temperature differences in aerosol dispersion, with implications for all indoor spaces. For instance, in hospitals, managing thermal gradients can enhance ventilation and air filtration systems, reducing airborne pathogen transmission. These insights support designing safer indoor environments and tailoring HVAC systems to minimize respiratory disease risks in critical public settings. Finally, the experimental data obtained in this study can be used to validate future computational fluid dynamics (CFD) simulations.

ACKNOWLEDGMENTS

This work was funded by Ministerio de Ciencia e Innovación MCIN (under projects I + D+i PID2020-113303GB-C21 and PID2023-146648NB-C21) and also by Departament d'Innovació Universitats i Empresa, de la Generalitat de Catalunya (under Project SGR-Cat_2021SGR00732). We also thank Francisco Belio

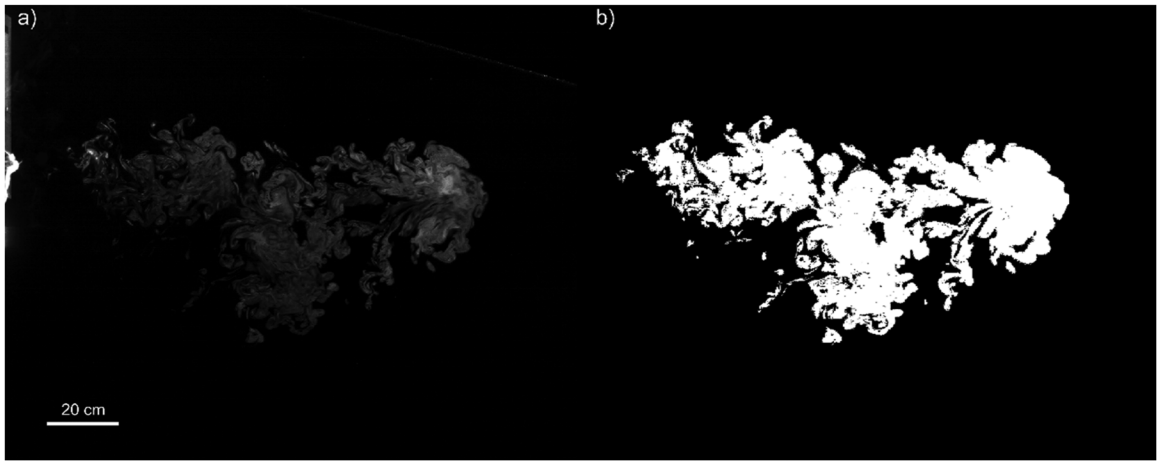

FIG. 14. Panel (a): raw image in one of the experiments. Panel (b): image postprocessed using binarized technique.

and Ivan Bellanco from Institut de Recerca en Energia de Catalunya (IREC) for their support and help in the use of the climate chamber.

AUTHOR DECLARATIONS

Conflict of Interest

The authors have no conflicts to disclose.

Author Contributions

Nicolás Catalán: Conceptualization (equal); Data curation (lead); Formal analysis (lead); Investigation (lead); Methodology (lead); Software (lead); Validation (lead); Visualization (lead); Writing – original draft (lead); Writing – review & editing (equal). **Salvatore Cito:** Conceptualization (lead); Formal analysis (equal); Funding acquisition (equal); Investigation (equal); Methodology (equal); Resources (equal); Supervision (lead); Writing – original draft (equal); Writing – review & editing (equal). **Sylvana Varela Ballesta:** Conceptualization (equal); Formal analysis (equal); Investigation (equal); Methodology (equal); Supervision (equal); Writing – review & editing (equal). **Alexandre Fabregat:** Conceptualization (equal); Formal analysis (equal); Investigation (equal); Supervision (equal); Writing – original draft (equal); Writing – review & editing (equal). **Anton Vernet:** Conceptualization (equal); Formal analysis (equal); Investigation (equal); Validation (equal); Writing – original draft (equal); Writing – review & editing (equal). **Daniel Graus:** Data curation (equal); Investigation (equal); Methodology (equal); Validation (equal); Visualization (equal); Writing – original draft (equal); Writing – review & editing (equal). **Jordi Pallares:** Conceptualization (lead); Formal analysis (equal); Funding acquisition (equal); Investigation (equal); Methodology (equal); Project administration (lead); Resources (equal); Supervision (lead); Validation (equal); Writing – original draft (equal); Writing – review & editing (lead).

DATA AVAILABILITY

The data that support the findings of this study are available from the corresponding author upon reasonable request.

APPENDIX A: IMAGE PROCESSING AND CALIBRATION

Figures 14(a) and 14(b) show the raw and binarized images, respectively. The threshold used for binarization was manually selected by performing an independence test, and its value was kept constant for each experiment. The particle cloud centroid was calculated from the binarized image, as described in Sec. II C. Calibration was performed independently for each experimental case. The camera was maintained in a fixed position, and calibration images were acquired using a reference object of known length placed within the field of view. The reference was positioned at different locations across the image in order to minimize perspective-related effects. The resulting measurements were averaged to obtain the meter-to-pixel conversion factor. Based on the dispersion of the calibration measurements, the maximum uncertainty in the centroid position was estimated to be $\pm$ 0.01 m. The characteristic centroid displacements observed in the experiments are on the order of 0.1 m (see Fig. 5), i.e., approximately one order of magnitude larger than the estimated measurement uncertainty, indicating that the reported trends are well above the measurement noise.

REFERENCES

[1]J. W. Tang *et al.*, "Airflow dynamics of human jets: sneezing and breathing—Potential sources of infectious aerosols," PLoS One **8**, e59970 (2013).
[2]V. Arumuru, J. Pasa, S. S. Samantaray, and V. S. Varma, "Breathing, virus transmission, and social distancing—An experimental visualization study," AIP Adv. **11**, 045205 (2021).
[3]C. C. Wang *et al.*, "Airborne transmission of respiratory viruses," Science **373**, eabd9149 (2021).
[4]N. Zhang *et al.*, "Close contact behavior in indoor environment and transmission of respiratory infection," Indoor Air **30**, 645–661 (2020).
[5]Z. Liu, H. Liu, R. Rong, and G. Cao, "Effect of a circulating nurse walking on airflow and bacteria-carrying particles in the operating room: An experimental and numerical study," Build. Environ. **186**, 107315 (2020).
[6]J. Wu, W. Weng, M. Fu, and Y. Li, "Numerical study of transient indoor airflow and virus-laden droplet dispersion: Impact of interactive human movement," Sci. Total Environ. **869**, 161750 (2023).
[7]J. K. Gupta, C. H. Lin, and Q. Chen, "Flow dynamics and characterization of a cough," Indoor Air **19**, 517–525 (2009).

[8]P. Bahl, C. M. de Silva, A. A. Chughtai, C. R. MacIntyre, and C. Doolan, "An experimental framework to capture the flow dynamics of droplets expelled by a sneeze," Exp. Fluids **61**, 176 (2020).
[9]M. Han *et al.*, "Experimental measurements of airflow features and velocity distribution exhaled from sneeze and speech using particle image velocimetry," Build. Environ. **205**, 108293 (2021).
[10]L. Bourouiba, E. Dehandschoewercker, and J. W. M. Bush, "Violent expiratory events: On coughing and sneezing," J. Fluid Mech. **745**, 537–563 (2014).
[11]P. Kant *et al.*, "Bag-mediated film atomization in a cough machine," Phys. Rev. Fluids **8**, 074802 (2023).
[12]A. C. K. Lai and S. L. Wong, "Expiratory aerosol transport in a scaled chamber under a variety of emission characteristics: An experimental study," Aerosol Sci. Technol. **45**, 909–917 (2011).
[13]L. Liu, J. Wei, Y. Li, and A. Ooi, "Evaporation and dispersion of respiratory droplets from coughing," Indoor Air **27**, 179–190 (2017).
[14]N. L. Phuong and K. Ito, "Investigation of flow pattern in upper human airway including oral and nasal inhalation by PIV and CFD," Build. Environ. **94**, 504–515 (2015).
[15]M. Auvinen, J. Kuula, T. Grönholm, M. Sühring, and A. Hellsten, "High-resolution large-eddy simulation of indoor turbulence and its effect on airborne transmission of respiratory pathogens - Model validation and infection probability analysis," Phys. Fluids **34**, 015124 (2022).
[16]A. Fabregat *et al.*, "Direct numerical simulation of the turbulent flow generated during a violent expiratory event," Phys. Fluids **33**, 035122 (2021).
[17]A. Fabregat *et al.*, "Direct numerical simulation of turbulent dispersion of evaporative aerosol clouds produced by an intense expiratory event," Phys. Fluids **33**, 033329 (2021).
[18]A. Monka, B. Fraga, D. Soper, and H. Hemida, "Influence of thermal stratification on the transport of polydispersed expiratory particles," Phys. Fluids **35**, 103304 (2023).
[19]A. Murga, R. Bale, C. G. Li, K. Ito, and M. Tsubokura, "Large eddy simulation of droplet transport and deposition in the human respiratory tract to evaluate inhalation risk," PLoS Comput. Biol. **19**, e1010972 (2023).
[20]J. Pallares, A. Fabregat, and S. Cito, "Effects of upper respiratory tract anatomy and head movement on the buoyant flow and particle dispersion generated in a violent expiratory event," J. Aerosol Sci. **166**, 106052 (2022).
[21]Z. Van Zante *et al.*, "A novel and versatile cough simulator for respiratory disease studies," Phys. Fluids **36**, 121907 (2024).
[22]N. Catalán *et al.*, "Effects of nasal cavity and exhalation dynamics on aerosol spread in simulated respiratory events," Phys. Fluids **36**, 123327 (2024).
[23]A. Lavrinenko, A. Fabregat, F. Gisbert, and J. Pallares, "Direct numerical simulation of pathogen-laden aerosol dispersion in buoyancy-driven turbulent flow within confined spaces," Int. Commun. Heat Mass Transfer **152**, 107272 (2024).
[24]G. Pei, M. Taylor, and D. Rim, "Human exposure to respiratory aerosols in a ventilated room: Effects of ventilation condition, emission mode, and social distancing," Sustainable Cities Soc. **73**, 103090 (2021).
[25]T. G. Foat *et al.*, "Modeling the effect of temperature and relative humidity on exposure to SARS-CoV-2 in a mechanically ventilated room," Indoor Air **32**, e13146 (2022).
[26]F. Liu, H. Qian, Z. Luo, S. Wang, and X. Zheng, "A laboratory study of the expiratory airflow and particle dispersion in the stratified indoor environment," Build. Environ. **180**, 106988 (2020).
[27]A. C. K. Lai and S. L. Wong, "Experimental investigation of exhaled aerosol transport under two ventilation systems," Aerosol Sci. Technol. **44**, 444–452 (2010).
[28]L. Liu, Y. Li, P. V. Nielsen, J. Wei, and R. L. Jensen, "Short-range airborne transmission of expiratory droplets between two people," Indoor Air **27**, 452–462 (2017).
[29]M. Allahyari, K. Liu, J. Salinas, N. Zgheib, and S. Balachandar, "Sensitivity of puff dynamics and airborne droplet nuclei distribution to variations in violent expiration events," Comput. Fluids **251**, 105758 (2023).
[30]X. Deng, G. Gong, and X. Yang, "Investigation of the effects of indoor air stability on the airborne transmission of droplets from violent respiratory events," Indoor Environ. **1**, 100036 (2024).
[31]J. Pallares *et al.*, "Numerical simulations of the flow and aerosol dispersion in a violent expiratory event: Outcomes of the '2022 International Computational Fluid Dynamics Challenge on violent expiratory events'," Phys. Fluids **35**, 045106 (2023).
[32]A. Grünebaum *et al.*, "How fever is defined in COVID-19 publications: A disturbing lack of precision," J. Perinat. Med. **49**, 255–261 (2021).
[33]M. C. Soteriou and A. F. Ghoniem, "Effects of the free-stream density ratio on free and forced spatially developing shear layers," Phys. Fluids **7**, 2036–2051 (1995).
[34]J. Pallares and A. Fabregat, "A model to predict the short-term turbulent indoor dispersion of small droplets and droplet nuclei released from coughs and sneezes," Indoor Built Environ. **31**, 1393–1404 (2022).
[35]N. Abani and R. D. Reitz, "Unsteady turbulent round jets and vortex motion," Phys. Fluids **19**, 125102 (2007).
[36]J. M. Richards, "Inclined buoyant puffs," J. Fluid Mech. **32**, 681 (1968).